

Observations of Entrainment in Eastern Pacific Marine Stratocumulus Using Three Conserved Scalars

IAN FALOONA,* DONALD H. LENSCHOW, AND TERESA CAMPOS

National Center for Atmospheric Research,⁺ Boulder, Colorado

B. STEVENS AND M. VAN ZANTEN

University of California, Los Angeles, Los Angeles, California

B. BLOMQUIST, D. THORNTON, AND ALAN BANDY

Drexel University, Philadelphia, Pennsylvania

HERMANN GERBER

Gerber Scientific, Reston, Virginia

(Manuscript received 18 August 2003, in final form 8 January 2005)

ABSTRACT

Fast measurements of three scalars, ozone, dimethyl sulfide (DMS), and total water, are used to investigate the entrainment process in the stratocumulus-topped boundary layer (STBL) observed over the eastern subtropical Pacific during the second Dynamics and Chemistry of Marine Stratocumulus Experiment (DYCOMS-II). Direct measurement of the flux profiles by eddy covariance is used to estimate the entrainment velocity, the average rate at which the boundary layer grows diabatically via incorporation of overlying free tropospheric air. The entrainment velocities observed over the course of the mission, which took place during July 2001, ranged from 0.12 to 0.72 cm s⁻¹, and appear to outpace the estimated large-scale subsidence as the boundary layer advects over warmer sea surface temperatures. Observed entrainment velocities display only a weak correlation with the buoyancy Richardson number defined at the inversion, which suggests that processes other than inversion strength, such as wind shear, might play a larger role in driving entrainment in the STBL than previously recognized.

This study is the first to use DMS as an entrainment tracer because the high-rate mass spectrometric technique has only recently been developed. The biogenic sulfur compound shows great promise for such investigations in marine environments because the free tropospheric concentrations are virtually nonexistent, and it therefore serves as an unambiguous marker of boundary layer air. As such, individual mixing events can be analyzed to determine the mixing fraction of boundary layer and free tropospheric air, and in several such cases buoyancy reversal was observed despite the absence of large-scale dissipation of the cloud field as postulated by cloud-top entrainment instability. Moreover, the redundancy attained in using three separate scalars allows for an investigation of the average height scales above the inversion from where air is blended into the STBL, and this tends to be less than 80 m above the mean inversion height, implying that the entrainment process occurs on very small scales.

* Current affiliation: Department of Land, Air, and Water Resources, University of California, Davis, Davis, California.

⁺ NCAR is sponsored by the National Science Foundation.

Corresponding author address: Dr. Ian Faloona, Dept. of Land, Air, and Water Resources, University of California, Davis, One Shields Avenue, Davis, CA 95616.
E-mail: icfaloona@ucdavis.edu

1. Introduction

A cursory examination of global satellite imagery, or even a transoceanic airplane flight, reveals the persistence of bright expanses of low-level marine stratocumulus. These cloud types are especially prevalent off western continental coasts in association with subtropical anticyclonic flows overlying the induced, cold oceanic upwelling. Such low altitude, high albedo clouds exert a negative climate forcing (i.e., net cooling effect) on the earth system because they radiate at temperatures similar to the surface, and yet reflect solar radiation effectively. A nebulous understanding of the mechanisms governing the development, maintenance, and dissipation of these clouds is considered one of the major impediments to accurate climate modeling (Hartmann 1998). Quite often the boundary layers that sustain these clouds are convectively activated by radiative cooling near their top, and much like a bowl of hot miso soup, will spontaneously develop wide, flat convection patterns. Unlike the conventional picture of a cloud-free boundary layer that entrains warmer air aloft in response to a strong surface buoyancy flux, the convection in these stratocumulus-topped boundary layers (STBLs) is strongly influenced by the entrainment fluxes, and in a sense the clouds control the mixing of the boundary layer. Quantification of the entrainment process and a better understanding of the regulating physical parameters are a necessity for accurate modeling of these stratiform clouds.

The second Dynamics and Chemistry of Marine Stratocumulus Experiment (DYCOMS-II) was a predominantly nocturnal field experiment that took place over the eastern subtropical Pacific (29°–32.5°N, 120.5°–123°W) during July 2001 on board the National Center for Atmospheric Research (NCAR) C-130 airborne laboratory. Most of the flights consisted of a series of Lagrangian circles approximately 60 km in diameter (30-min flight time) at several levels within the STBL along with flight circles well above the capping thermal inversion to characterize the free tropospheric air and delineate STBL structure remotely via the NCAR nadir-looking lidar, the Wyoming cloud radar, as well as dropsondes. At either end of the on-station flight segment, a remote leg was flown at an altitude exceeding 2 km MSL, and one took place in the middle of the flight at an average of 300 m above the mean inversion height. During each leg the aircraft was advected by the local winds; thus because of shear (particularly above the inversion) the Lagrangian objectives were not met exactly. A detailed overview of the mission along with some preliminary results can be found in Stevens et al. (2003a).

The following work advances new, and what we believe to be more accurate, observations of the entrainment rates in marine stratocumulus by bringing to bear novel observations of dimethyl sulfide (DMS), a particularly apt scalar for tracking marine boundary layer (MBL) air. Considerable attention is given to the sources of measurement error expected during the experiment, while eliminating as many avenues of systematic error as possible. The estimated random errors are propagated through the calculations to derive reasonable uncertainties in the entrainment rates. The conceptual model upon which the technique is based is summarized in the following section, and the small but nonnegligible influences of chemical reactivity are addressed. Then the redundancy of using three separate scalars to measure the same quantity simultaneously is shown to have additional benefits in studying the details of the entrainment process itself.

2. Theoretical method

The theoretical foundation of stratocumulus-topped mixed layers was first expounded in the seminal work of Lilly (1968), and much of the approach herein derives from that study. The scalar concentrations are considered to be well mixed within the STBL and then jump discontinuously across the cloud-top interface. The scalar budget equation describing the temporal change of the mean scalar field, S , in a horizontally homogenous turbulent medium is

$$\frac{\partial S}{\partial t} + W \frac{\partial S}{\partial z} = - \frac{\partial \overline{w's'}}{\partial z} + Q, \quad (1)$$

where W is the mean vertical velocity (we will use the convention of uppercase representing mean thermodynamic quantities throughout), s' is the fluctuating scalar concentration, thus $\overline{w's'}$ is its turbulent flux, and Q is the net of in situ production and loss. Here we neglect the horizontal advection terms because of the Lagrangian sampling strategy of the experiment. We do not expect any rapid in situ photochemistry, particularly at night, and thus the Q term is ignored for O_3 and DMS; however, in situ estimates of drizzle are used as sinks for total liquid water. The boundary layer growth can be described as the sum of entrainment and mean vertical motion,

$$\frac{\partial z_i}{\partial t} = w_e + W, \quad (2)$$

where the quantity we are interested in, the entrainment velocity, w_e , quantifies the rate at which turbulence incorporates air into the boundary layer from aloft. The previous two equations can thus be related by integrating (1) across the inversion at z_i , allowing the

interface to be vanishingly thin, employing Leibnitz's rule, and realizing that the scalar fluxes vanish above the inversion. Then the entrainment velocity is related to the scalar budget of a conserved species with insignificant cloud-top sources/sinks by

$$w_e = \frac{-\overline{w's'}|_{z_i}}{\Delta S}, \quad (3)$$

where ΔS is the difference between the concentration in the overlying air and that in the boundary layer, and $\overline{w's'}|_{z_i}$ is the turbulent flux of the scalar at the inversion height. This deceptively simple relationship can be used to make direct observations of the entrainment velocity by measuring fluxes of chemical constituents throughout the boundary layer along with their jump across the inversion; however, this ratio or flux-jump method is not entirely free of difficulties.

Because flux measurements are nearly impossible to make exactly at the inversion height, we measured at multiple levels within the STBL and extrapolated a linear profile to the mean height of the inversion determined from a composite of the in situ data. Implicit in this technique is the assumption that the flux profiles are linear, which one expects for the quasi-steady conditions observed during DYCOMS-II (Stevens et al. 2003b) but may not be the case if the scalar possesses any vertically varying internal sources or sinks. Moreover, the fluxes are assumed to be constant over the duration of a flight (typically 5–6 h on station.) These complications were ameliorated during DYCOMS-II due to the nocturnal nature of most flights. The absence of solar radiation greatly simplifies the chemical budgets because in such low NO_x environments as the remote marine boundary layer, extremely slow production rates of OH and NO_3 radicals are expected (Tanner and Eisele 1995; Platt et al. 1990); thus, chemical activity should remain virtually in stasis overnight. However, it is known from laboratory studies (Lee and Zhou 1994) that reaction between dissolved DMS and O_3 does occur in aqueous systems such as stratocumulus cloud droplets. Fortunately, the principal controls on this reaction rate, namely temperature, liquid water content, and the gas phase reactant concentrations, were all monitored during DYCOMS-II. The correction method for this additional chemical sink is outlined in the following section.

The other complication in using Eq. (3) to measure entrainment is the assumption that there is a well-defined jump in the scalar concentration. Past observational studies of STBL entrainment have employed the ratio method using total water and ozone with mixed success (Kawa and Pearson 1989a; Bretherton et al. 1995) and usually very large data scatter. The relatively

long lifetimes of ozone and water (~ 1 week in this region of the atmosphere) in conjunction with their varied sources lead to substantial horizontal variability in the free troposphere, frequently accompanied by a complex vertical structure directly above the inversion. Thus the exact jump is often ill defined for these two species. DMS, on the other hand, is an almost ideal tracer of MBL air because its only source is at the ocean surface and its chemical lifetime (1–3 days) is comparable to the dilution time scale of the MBL due to entrainment (Lenschow et al. 1999).

3. Experimental method

a. Ozone

Ozone is a ubiquitous and extremely reactive component of the earth's troposphere. The chemical steady state is maintained globally by an influx from the stratosphere and a deposition at the surface but, in between, controls of its abundance are myriad and complex, dependent primarily on the availability of oxides of nitrogen ($\text{NO}_x = \text{NO} + \text{NO}_2$), and volatile organic compounds (VOCs). There is a great difference between the way these factors play themselves out in marine, as opposed to terrestrial, environments, more so even than the interhemispheric difference (Crutzen et al. 1999). Conventionally it is believed that the budget of ozone in the MBL is that of gradual buildup overnight via entrainment from ozone-rich layers aloft, balanced by photochemical destruction during the day in conjunction with a continuous yet gradual loss to the ocean surface. This paradigm was generally upheld by the Lagrangian observations during DYCOMS-II.

Ozone was measured on board the C-130 by a NO chemiluminescence instrument built at NCAR's Research Aviation Facility. A very similar instrumental design is described by Pearson (1990). Our instrument operated at sample flow rates in excess of 10 slpm (standard liters per minute) and at an internal pressure of about 10 hPa. Air is pulled into a gold-plated cylindrical reaction chamber and mixed with a small flow of NO. A portion of the resultant NO_2 is produced in an electronically excited quantum state and spontaneously emits light in the red to near-infrared region of the electromagnetic spectrum (Ridley 1978). This chemiluminescence is measured by a photomultiplier tube chilled in dry ice to reduce its background response to thermal radiation. Because of its molecular polarizability and atmospheric abundance, water vapor acutely quenches such electronically excited species. In order for chemiluminescence to proceed efficiently, the NO_2 excited state needs to exist long enough for it to spontaneously emit a photon, and the more water vapor in

the sample air, the more rapidly it is deactivated by molecular collisions, bypassing the decay route of photon emission.

A slightly modified commercial ozone analyzer, a ThermoElectric Instruments 49C unit, which uses the more commonplace UV absorbance technique, was operated alongside the fast instrument with a typical response time of ~ 10 s. The data from both instruments were digitally filtered down to 30-s sampling rates, the inlet delays corrected for, and then a multiple regression was carried out to fit the operating parameters of the chemiluminescence measurement to a best-fit sensitivity function. Taken as a whole the standard deviations of these fits were typically around 2% for each flight. Although we did not quantify the water quenching effect in the laboratory with this exact instrument, the influence is thought to be well understood and relatively mild. Two values exist in the literature for this quenching coefficient (Mathews et al. 1977; Ridley et al. 1992), and they differ from one another by about 30%. We used the Mathews et al. (1977) value because it provided a better fit of the calibration data, and minimal correlation of the residuals with water vapor concentration. Nonetheless, the difference in the coefficients could represent a systematic error in the ozone measurement, so it is a worthwhile exercise to estimate its effect on the ozone vertical flux.

The influence of this water vapor correction on an ozone flux measurement can be considered in terms of a ratio of water vapor to ozone fluxes:

$$\frac{\overline{w'q'}}{\overline{w'o_3'}} = \frac{r_{wq}\sigma_w\sigma_q}{r_{wo_3}\sigma_w\sigma_{o_3}}, \quad (4)$$

where the water and ozone fluxes are represented by their correlation coefficients, r_{wq} and r_{wo_3} , and σ_w , the standard deviation of the vertical wind, as well as the standard deviations of water and ozone, σ_q and σ_{o_3} . The correlation coefficients for humidity typically fall between 0.3 and 0.6, depending on height within the STBL, while those for ozone usually range from -0.1 to -0.4 . The variance generated by an ambient humidity flux could then leak into the variance measured in the ozone signal. The difference between the two literature values for the water correction to the ozone signal is about $0.0015 \text{ g}^{-1} \text{ kg}^{-1}$, thus a conservative estimate of the magnitude of a spurious ozone variance, σ'_{o_3} , is given by the product of this correction factor and the standard deviation of water vapor. The relative contribution of this error to the total ozone flux then becomes $r_{wq}\sigma'_{o_3}/r_{wo_3}\sigma_{o_3}$. For conditions encountered during DYCOMS-II, this relative bias might range from 2% to 8% of the ozone flux signal, being largest near the ocean surface where the correlation between vertical

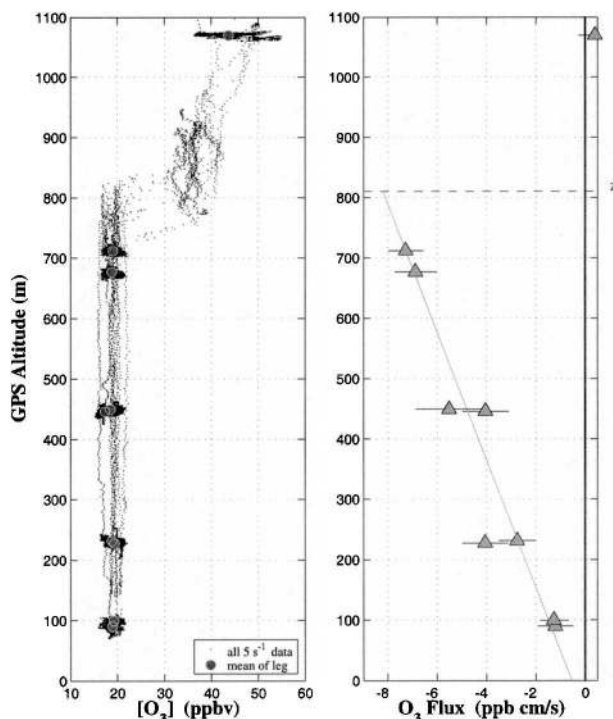


FIG. 1. (left) Ozone data collected on station during research flight 7 (RF07), averaged to 5 s^{-1} (small dots), and the averages (filled circles) for each leg. (right) The mean fluxes measured on each 30-min leg along with the standard deviation of the mean of the 2.5-min (15 km) sublegs. The line is the weighted least squares fit through the fluxes, and the extrapolation to the inversion height is used in Eq. (3) to estimate the entrainment velocity.

wind and humidity is greatest but that with ozone is smallest. We emphasize that this represents the largest plausible water interference that might exist, and we expect that it is, in fact, much smaller.

Figure 1 shows a compilation of the ozone data (left panel), filtered to a sampling rate of 5 s^{-1} , collected on station as a function of altitude from research flight 7 (RF07). The right panel of Fig. 1 shows the observed vertical fluxes of ozone, one from each of the circular, 30-min flight legs. Figure 1 appears consistent with the traditional idea of the diurnal cycle of remote MBL ozone in low- NO_x environments (Liu et al. 1983); namely, an entrainment of ozone rich air from the free troposphere and a slow deposition at the ocean surface resulting in a buildup of ozone in the boundary layer overnight. This is believed to be compensated by net photochemical destruction during the daytime, and applying a scalar budget of the form of Eq. (1) to the one daytime flight, RF08, indicates that there is indeed a net ozone loss of approximately 1.5 ppb day^{-1} . The magnitude of this loss is in agreement with other estimates in this region (Kawa and Pearson 1989b; Paluch et al.

1994) and corroborates our assumption that the study area was one of low background NO_x concentrations.

b. Dimethyl sulfide

DMS is a key component of the earth's sulfur cycle, and its main source is from oceanic phytoplankton (Watts 2000). This reduced sulfur species is highly susceptible to attack by the hydroxyl radical, the principal atmospheric oxidant generated by UV radiation, and consequently has a chemical lifetime of approximately 1–3 days in the remote MBL at midlatitudes. A chemical time scale of this magnitude is much longer than a characteristic eddy-turnover time within the STBL (~ 15 min), while being short with respect to the average time of convective injection into the free troposphere and subsequent advection to the study area. The latter time scale is at least as long as the mean time of exchange between the STBL and free troposphere, approximately a boundary layer depth, z_b , divided by an entrainment velocity, w_e , ($1000 \text{ m}/0.005 \text{ m s}^{-1} \sim 2.5$ days). Consequently DMS is both well mixed throughout the STBL and falls to near zero above, making it uniquely suited as a tracer of STBL air. The compilation of all 5 s^{-1} data collected on station during RF07 illustrates this feature quite clearly in Fig. 2 (left panel). The DMS flux profile is shown in the right panel of Fig. 2 from direct eddy correlation measurements of the covariance between the DMS signal and the vertical winds. DYCOMS-II was the first time that fast measurements of this analyte (Bandy et al. 2002) have been brought to bear on issues of scalar entrainment and mixing in the atmosphere.

While the data in Fig. 2 demonstrate a clearly defined jump in DMS between the STBL and the free troposphere, they also illustrate the large horizontal variability encountered during most of the flights. The DMS concentrations on either side of the 60-km diameter flight legs varied by as much as a factor of 2, and the mean horizontal gradients sampled during DYCOMS-II ranged from 0.2 to 0.6 ppt km^{-1} . The cause of such strong gradients remains unknown but may be due to heterogeneous source patterns in the ocean surface, or horizontal variability in entrainment rate, or both. Due to these strong gradients, any deviation in the Lagrangian circuit of the aircraft throughout the night had a significant impact on the mean leg concentration and consequently complicates the evaluation of subtle vertical gradients and time rates of change in the mixed layer.

A detailed study of the chemical budgets and their closure will be presented in a separate paper; here we focus on some of the complications of these tracers that might introduce systematic errors into our estimates of

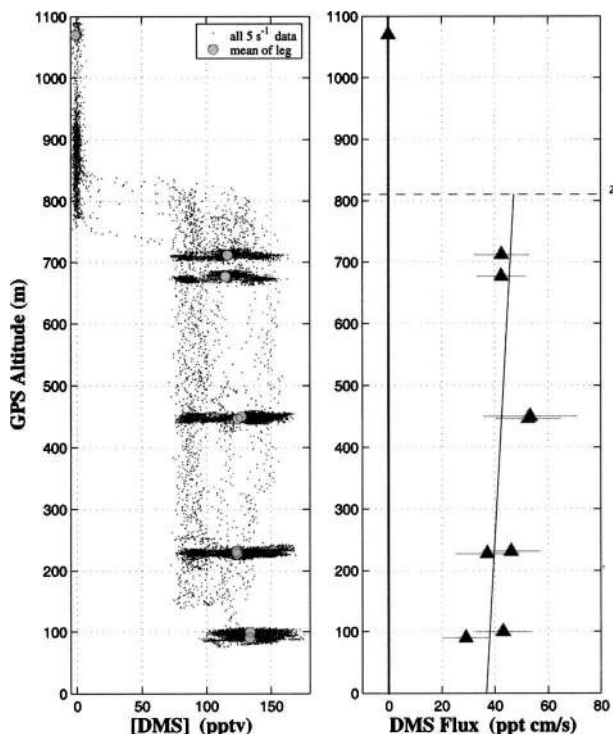


FIG. 2. As in Fig. 1 but for DMS.

entrainment. For DMS there is the problem of the aforementioned aqueous loss by reaction with dissolved ozone in the stratocumulus droplets. The influence of this nocturnal chemical loss on the flux profile can be ascertained by taking the derivative of Eq. (1) with respect to height and neglecting any mean vertical accelerations to derive

$$\frac{\partial}{\partial t} \frac{\partial S}{\partial z} = - \frac{\partial^2 \overline{w's'}}{\partial z^2} - \frac{\partial L_{\text{aq}}}{\partial z}. \quad (5)$$

Here L_{aq} is the aqueous loss rate of DMS in the cloud water. Assuming that the turbulence structure is in quasi-steady state, the vertical gradients of the mean quantities should be constant in time; therefore, the left-hand side of Eq. (5) is zero and the curvature of the flux profile is balanced by the negative gradient of the chemical loss term. The aqueous reaction rate between ozone and DMS (Gershenson et al. 2001) can be represented as

$$L_{\text{aq}} = (RT)^2 H_{\text{O}_3} H_{\text{DMS}} \text{LWC} [\text{O}_3] [\text{DMS}] k_{\text{aq}}(T), \quad (6)$$

where R represents the universal gas constant, T is the temperature of the cloud water, H_{O_3} and H_{DMS} are the Henry's Law coefficients that determine how much of the gas phase ozone and DMS, $[\text{O}_3]$ and $[\text{DMS}]$, respectively, partition into the liquid phase, LWC is the frac-

tional liquid water content, and $k_{aq}(T)$ is the reaction rate coefficient, which is a weak function of temperature. Because the stratocumulus studied in DYCOMS-II were only 200–500 m deep, and consequently the temperature change across the cloud was only on the order of 1–2 K, the primary agent responsible for the gradient of the aqueous loss term is the liquid water content of the cloud, which tended to be very close to that expected from adiabatic condensation.

It is worthwhile to note that the time scale of gaseous diffusion to a droplet in these conditions (radius $\sim 10 \mu\text{m}$, surface area concentration $\sim 0.1 \text{ m}^{-1}$) is on the order of 5 s, so the loss process should be readily equilibrated while mixing throughout the cloud. Furthermore, the overall lifetime of DMS with respect to this aqueous loss term was typically greater than one week, much longer than the mixing time of the STBL, therefore the Damköhler number (the ratio of chemical to turbulent time scales) is much greater than unity and reactant covariances are not expected to complicate Eq. (6) significantly.

The greatest control of this chemical reaction correction term comes from the mean DMS concentration, which is often correlated with the magnitude of the fluxes themselves. Thus, although there appears to be a broad range in this effect (2–15 ppt cm s^{-1}), it is usually less than a 10% relative effect on the fluxes near cloud top. For all of the flux profiles used in this study, the in-cloud fluxes were explicitly corrected for this curvature effect and then a linear fit of the resultant flux profile was made to extrapolate to the inversion base.

The other vulnerable assumption for DMS is that the flux profile is constant during each flight. While the direct measurement of DMS fluxes are in their infancy, diurnal measurements made in marine environments (Bandy et al. 1996; Kouvarakis and Mihalopoulos 2002) seem to indicate the absence of drastic changes in DMS emission rates overnight; however, these studies tend to be poorly constrained by observations of MBL-free troposphere exchange, and can only be invoked loosely to bolster the constant flux assumption. Nonetheless, the Lagrangian air mass under study during DYCOMS-II tends to advect over at least 100 km while being sampled and such a distance might cover substantial gradients in the ocean surface DMS concentration and consequently the flux. Fortunately, the oceanic fluxes have the least influence on the extrapolation to the inversion height. A simple test of the sensitivity was performed by increasing the uncertainty of the surface fluxes fourfold, which affected the resultant flux at the inversion height less than 5%. Finally, the fast atmospheric pressure ionization mass spectrometer (APIMS) instrument rapidly dries and heats the inlet air to con-

stant humidity conditions where the proton transfer reaction occurs (Bandy et al. 2002), thereby rendering the measurement insensitive to water and thus uninfluenced by water fluxes.

c. Total water

The total water variable, q_t , was derived from the sum of the NCAR C-130 cross-flow Lyman- α hygrometer measurement of water vapor (q_v) and, when in cloud, the Gerber PVM-100 optical droplet detector, q_l ($q_t = q_v + q_l$). The latter is reported in g m^{-3} , so the fast-response measurements of air density are used to convert to g (liquid)/kg(dry air). The cross-flow Lyman- α performed well throughout the mission and did not appear to be strongly affected by wetting in clouds. The absolute value of the fast humidity measurement is tied to the slower General Eastern Model 1011B dew-point hygrometer on longer time scales. The total water flux calculated with this variable and used to estimate the entrainment needs to be augmented with the drizzle flux in order to represent a conserved variable. The drizzle fluxes were estimated from the product of the mean drop size distributions and calculated Stokes velocities (van Zanten et al. 2005) and then subtracted from the mean total water flux on each leg.

d. Eddy correlation

Each of the three scalars was sampled synchronously at 25 s^{-1} along with the vertical wind from the gust probe. Perusal of the cospectra of the scalars with the vertical wind lead us to determine that a good high-pass filter length for all of the data was 2.5 min, or approximately 15 km along the flight path. The choice was made based on the average zero-crossing of the scalar and vertical wind cospectra at the low wavenumber end, and the filter edge typically fell a factor of 10–20 beyond the cospectral peak. We feel that this filter size represents the best choice in capturing all the relevant scales of motion influencing the scalar STBL fluxes while eliminating most mesoscale contributions that should contribute randomly and are assumed to be irrelevant to the entrainment process. An interesting feature of the DMS cospectra appeared in comparing the peaks at different altitudes within the boundary layer. On each flight, the cospectral peak for DMS shifted out toward larger scales, 5–10 km, in the middle of the STBL. This is consistent with the size of the wide convective circulations observed in other measurements such as the University of Wyoming Cloud Radar (D. Leon 2003, personal communication), and required the use of a large enough spectral filter to include this consistent feature of the DMS fluxes. Similar cospectral

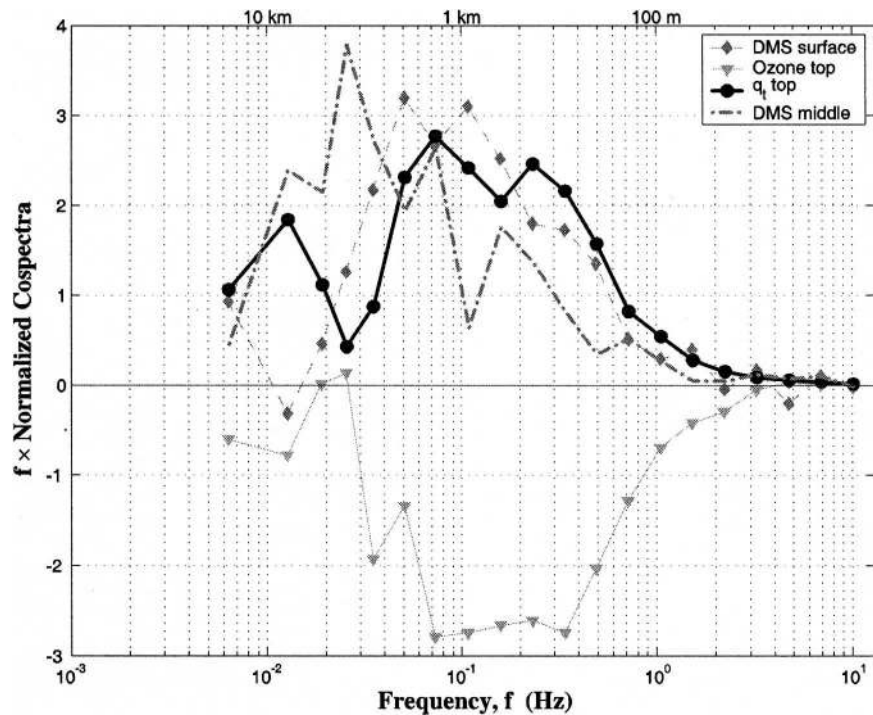


FIG. 3. Normalized cospectra of vertical wind and the three scalars from RF02. Because the flight speed was very near 100 m s^{-1} throughout the mission, a spatial scale is included on the top axis. The ozone and total water cospectra are for one hour of data collected near cloud top, and the two DMS cospectra come from the surface and the middle legs, indicating the increase in spatial scales carrying the flux in the center of the STBL.

features appear with q_t and O_3 as well, but not quite as dramatically as with DMS.

After removal of the mean and linear trend, the covariance was calculated for each 2.5-min segment with each overlapping half of the neighboring interval. Most of the level flight legs were 30 minutes in duration so they comprise ~ 24 subleg covariance calculations, which were averaged together to derive the full leg flux. Any of the sublegs containing missing data were ignored in the determination of the covariance. The error bars in Figs. 1 and 2 represent the standard deviation of the mean for the ~ 12 independent (i.e., nonoverlapping) subleg measurements. Examples of the cospectra of all three of the scalars, normalized by their respective fluxes, from RF02 are shown in Fig. 3. The cospectra of O_3 and q_t represent the averages over the two uppermost legs during the flight, which were positioned approximately 100 m below the inversion, while the DMS cospectrum is from the surface leg. The additional DMS cospectrum, however, was measured in the middle of the STBL ($z/z_i \sim 0.65$) and shows the inclusion of larger scale motions in the turbulent transport of DMS up from the ocean surface, as discussed above. Although the absolute measurements of ozone and DMS become more and more compromised by noise at

high frequencies, the noise is Poisson and thus white in nature and as such is not correlated with the vertical winds. When this type of instrumental noise is averaged sufficiently over the course of a full leg, the resultant cospectra (Fig. 3) show that the covariance is accurately captured by these two instruments because they mimic that of the total water variable quite closely.

e. Subsidence and the growth of the STBL

Entrainment rates can also be derived by relying on the balance represented in Eq. (2) and measuring the growth rate of the boundary layer height and the large-scale subsidence rate (Stevens et al. 2003a). While the details of deriving the divergence from the flight data (and thus inferring the subsidence rate from continuity) are still being worked out, we resort here to three model datasets for an estimate of the mean vertical velocity (and an idea of its variance). We used the output from the 48-h Aviation Model (AVN) from the National Centers for Environmental Prediction (NCEP), as well as two products from the European Centre for Medium-Range Weather Forecasts (ECMWF): the 72-h Diagnostique des Domaines Horizontaux (DDH) operational forecast model and the 40-yr ECMWF Re-Analysis (ERA-40) datasets. In

each case the semidiurnal tide was removed by subtracting the surface pressure tendency (typically less than a 10% correction.) The vertical velocities exhibited very small vertical gradients and the inversion heights observed during the mission only ranged from 900 to 945 hPa. Therefore, the values at the nearest model level (900 or 925 hPa) were averaged over a 12-h period encompassing the flight, representing a $2.5^\circ \times 2.5^\circ$ box containing the entire study region. Figure 4 shows how the observed entrainment rate as derived by the flux-jump method from DMS corresponds to the three models' subsidence rates. The scatter in the subsidence rates is at times very large (the mean standard deviation among the three models is 0.16 cm s^{-1}), but the data indicate that the entrainment rates, in general, exceed the magnitude of the synoptic-scale subsidence. This observation is consistent with the picture of an STBL advecting equatorward over increasing sea surface temperatures leading to increased surface fluxes and a deepening boundary layer (Schubert et al. 1979).

We estimate the growth rate of the STBL by using a mélange of both the downward looking lidar data from the NCAR Scanning Aerosol Backscatter Lidar (SABL) and the in situ DMS data during the porpoising leg if such a leg were flown. The former method relies on the cloud-top reflectivity as an estimate of the boundary layer height and is an average of 1-s range data from the lidar subtracted from the GPS altitude. The cloud-top height is not included in the average, if the lidar return comes from below the mean cloud base (as determined from averages of the in situ liquid water probe), because these data represent breaks in the cloud cover and not extreme drops in the boundary layer height. The latter method relies on the fact that DMS is such a clean delimiter of MBL air: the altitudes of both rising and falling edges of the porpoising DMS record are averaged together to derive a mean interfacial height for the leg.

The standard deviations of both methods were similar and typically ranged between 20 and 50 m across the 60 km diameter leg. This variability corresponds qualitatively with the standard deviation of cloud-top heights of 20 m derived from large eddy simulations of the STBL for the conditions of RF01, albeit on a somewhat smaller spatial domain of 5 km (C.-H. Moeng 2003, personal communication). The estimates of mean boundary layer height from each of the legs, from two to four over the course of each flight, and their standard deviations then went into a weighted least squares fit to come up with the growth rate of the boundary layer. The average standard deviation of the growth rates was 0.31 cm s^{-1} and added in quadrature with the same for the model subsidence values yields an approximate $1\text{-}\sigma$

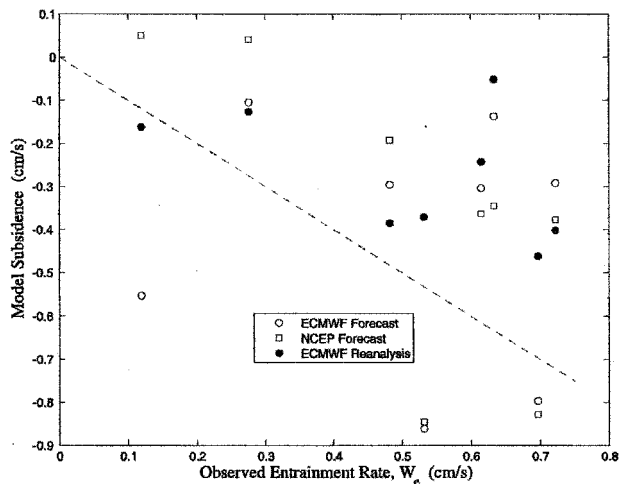


FIG. 4. The observed entrainment velocities (determined from the DMS method) and the three model estimates of mean vertical velocities. The dashed line is the 1 to -1 line representing a boundary layer in equilibrium [Eq. (2)].

error of 0.35 cm s^{-1} for this method. Because two of these legs were advected by the local winds above 2.5 km, which were often quite different from the boundary layer winds, caution was required to ensure that observations being made of the secular change were not contaminated by spatial inhomogeneities in the large-scale cloud height field.

4. Entrainment velocities

One of the primary objectives of DYCOMS-II was to use the observations to estimate the entrainment velocity, w_e , of the STBL by as many independent techniques as possible. This built-in redundancy of the experiment has helped to elucidate some of the suspected strengths and weaknesses of the various methods. Many previous studies have used the ratio method for ozone and water (e.g., Kawa and Pearson 1989a; Bretherton et al. 1995; de Roode and Duynkerke 1997), but the vertical structure of these two scalars tends to be quite variable and highly layered above the inversion (Kawa and Pearson 1989b). Furthermore, shortwave radiation effects can complicate this type of analysis because the forcing is heterogeneous in space and time and the induced heating near the top of the STBL can often lead to cloud layer decoupling (Turton and Nicholls 1987). Thus, not only did the nocturnal setting of the DYCOMS-II experiment simplify the chemical budgets due to the absence of photochemical activity, it also allowed for observations under the much simpler thermodynamic condition of no shortwave heating.

Table 1 lists some of the characteristics of each flight

TABLE 1. Environmental characteristics of the stratocumulus-topped boundary layers encountered during DYCOMS-II. RF08 is divided into two sections representing the day (bold) and night portions of the flight. Averages are for the nocturnal flights only.

Flight number	w_* (m s ⁻¹)	Θ_v jump (K)	Q_t jump (g kg ⁻¹)	O ₃ jump (ppbv)	Buoyancy Ri _{w*}	Wind shear (m s ⁻¹)	Cloud base (m)	Max. LWC (g m ⁻³)	Est. drizzle (mm day ⁻¹)	z_i (m)
RF01*	1.05	10.5	-7.8	23.5	268	3.8	560	0.4	0.05	830
RF02*	1.01	6.3	-5.2	14.2	161	3.7	380	0.6	1.02	770
RF03	1.13	7.4	-6.8	-11.5	127	2.4	220	0.7	0.21	650
RF04	1.08	5.4	-4.4	9.6	167	3.4	580	0.9	0.60	1070
RF05*	1.13	7.5	-6.8	15.3	179	4.3	680	0.0	0.01	910
RF07	1.03	7.0	-6.3	24.6	181	1.4	320	0.8	1.10	810
RF08a	0.51	11.3	-7.5	18.6	884	1.5	220	0.5	0.54	610
RF08b	0.81	10.2	-7.5	18.8	334	1.5	260	0.7	0.44	630
Nocturnal averages	1.03	7.8	-6.4	13.5	202	2.9	429	0.6	0.5	810

* Indicates definite instability with respect to cloud-top entrainment according to Randall–Deardorff criterion.

and Fig. 5 illustrates typical thermodynamic profiles from RF07. The generalized convective velocity scale, w_* , of Deardorff (1980) is calculated from a trapezoidal numerical integration of the buoyancy fluxes measured throughout the STBL:

$$w_*^3 = 2.5 \frac{g}{\theta_v} \int_0^{z_i} \overline{w' \theta_v'} dz, \quad (7)$$

where the factor of 2.5 is an ad hoc coefficient that forces w_* to approximately converge to the convective velocity scale for the clear air boundary layer. The buoyancy Richardson number, Ri_{w*}, is defined using the convective velocity scale by

$$\text{Ri}_{w_*} = \frac{g}{\theta_v} z_i \Delta \theta_v / w_*^2, \quad (8)$$

where g is the gravitational constant, θ_v is the mean virtual potential temperature, and $\Delta \theta_v$ is the jump across the inversion. The virtual potential temperature jump is defined as the difference between the two altitude bins below and above where the lapse rate is greater than 3.5 K (100 km)⁻¹. The inversion height, z_i , is defined as the bottom of the 20-m altitude bin that exhibits the greatest lapse rate in the mean profile calculated from all the 5 s⁻¹ data measured on station. The mean inversion height thus derived matched other estimates made throughout the course of each flight as well as measurements of cloud top made by the lidar to within 20–40 m. Research flight 8 was split into two separate sections (RF08a and RF08b) because the first half occurred during daytime conditions (approximately 1400–1630 LST) and the second half occurred under nighttime conditions (1700–1930 LST, solar zenith angles from 65° to 100°).

The entrainment velocities derived from each of the three scalars, using the ratio method of Eq. (3), and

from the STBL growth and subsidence rate estimates Eq. (2) are summarized in Table 2 for the seven Lagrangian flights that were tailored to study entrainment. The 1- σ standard deviations reported for each scalar entrainment velocity are conservative estimates based on a propagation of random errors through the calculations using Eq. (3).

a. Random and systematic errors

The two main sources of random error in the ratio method are, first, that incurred from the extrapolation of the flux profile to the inversion height. Each flux profile is fit to a line by a least squares linear regression, weighted by the standard deviation of the mean of each flux leg. This assumes that any variability in the fluxes within each leg arises solely from random turbulent fluctuations and does not represent any physical horizontal gradients in the vertical flux field (i.e., the horizontal homogeneity assumption). The independent variable is taken to be $(z_i - z)$ such that the y intercept represents the flux at the mean inversion height, and the uncertainty in the y intercept is estimated from the weighted least squares fit. The second comes from imprecision in the measurements of the mean concentrations and the resultant error in the jump estimate. We use the standard deviation of the mean of all 30-min legs within the STBL in conjunction with the standard deviation of the 30 min above cloud leg to derive the error in the jump. In the case of ozone, the horizontal spread in the free-tropospheric concentrations above cloud contributes the most to the overall error, while for water vapor it is comparable to the flux extrapolation error, and for DMS it is entirely insignificant. However, the error in the jump is much more prone to systematic errors (in the case of ozone and humidity) due to insufficient sampling of the entrainment zone and

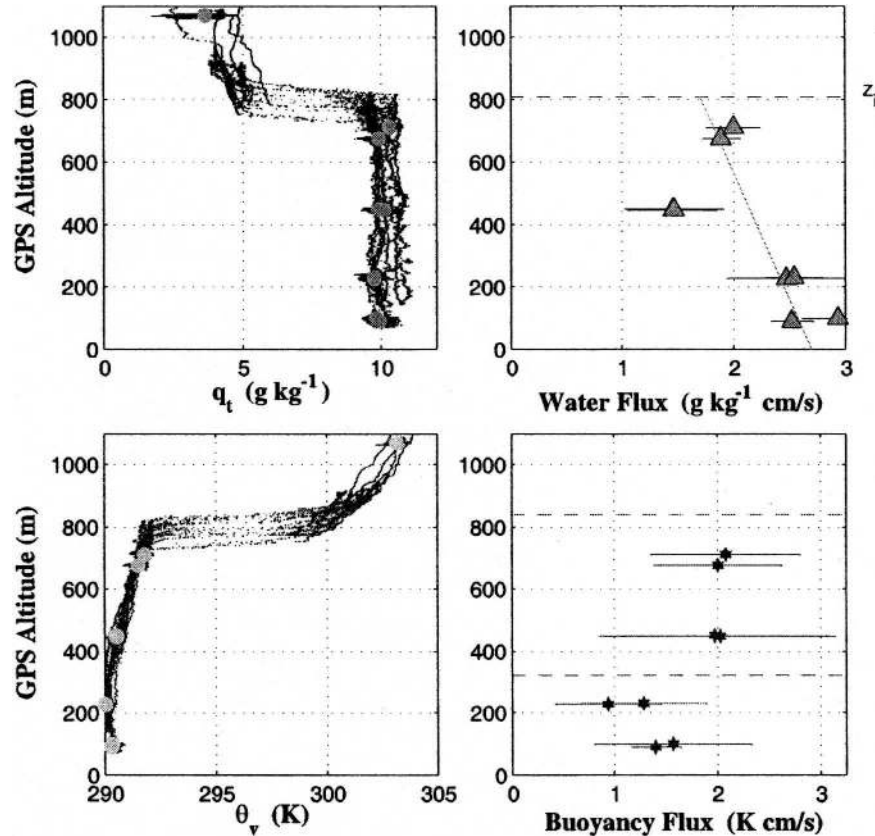


FIG. 5. Thermodynamic profiles from RF07. (left) The panels show the 5 s^{-1} data (small points) collected on station along with each leg average (filled circles). (right) The fluxes along with the standard deviations from each flight leg and the weighted linear fit. The horizontal dashed lines depict the inversion height and average cloud base.

wind shear across the inversion, which will cause differential advection to continually change the conditions of the free-tropospheric air mass.

The entrainment fluxes of DMS measured near the top of the STBL tend to be correlated with the mean

concentration field, with correlation coefficients ranging from 0.15–0.45 (the one daytime flight shows a negative correlation of -0.30). Such strong correlations seem to indicate that the entrainment rate is relatively uniform across the domain of the experiment and

TABLE 2. Entrainment velocities derived from the four separate techniques during DYCOMS-II. RF08 is divided into two sections representing the day (bold) and night portions of the flight. Averages are for the nocturnal flights only.

Flight number	dz_i/dt (cm s^{-1})	W (cm s^{-1})	$dz_i/dt - W$ (cm s^{-1})	DMS		Total water, Q_t		Ozone, O_3	
				w_e (cm s^{-1})	1σ	w_e (cm s^{-1})	1σ	w_e (cm s^{-1})	1σ
RF01	0.06	-0.69	0.75	0.53	0.10	0.35	0.03	0.26	0.09
RF02	0.06	-0.70	0.76	0.70	0.15	0.64	0.17	0.60	0.17
RF03	0.21	-0.36	0.57	0.72	0.09	0.40	0.06	0.67	0.20
RF04	0.00	-0.18	0.18	0.63	0.11	0.38	0.11	0.22	0.09
RF05	-0.08	-0.30	0.22	0.61	0.07	0.58	0.05	0.56	0.12
RF07	0.00	-0.29	0.29	0.48	0.06	0.27	0.04	0.33	0.06
RF08a	NaN	-0.22	NaN	0.12	0.12	-0.04	0.03	0.00	0.03
RF08b	-0.18	-0.06	-0.12	0.28	0.07	0.21	0.03	0.15	0.08
Nocturnal averages	0.01	-0.37	0.38	0.57	0.09	0.41	0.07	0.40	0.12

points to an inhomogeneous surface source as the root cause of the large horizontal DMS gradients observed. Furthermore, because of the positive correlation between the numerator and denominator in Eq. (3), the error estimate of the entrainment velocity for DMS is appropriately reduced.

Because of the mesoscale variability in STBL height and the difficulties in monitoring it in an accurate, Lagrangian manner over the course of the flight, the relative error estimates for the boundary layer growth rate are the largest. As discussed in Stevens et al. (2003b) for RF01, despite the large data scatter, the boundary layer did not appear to grow substantially over the course of the flight and the same holds true for all of the observed STBL growth rates—all are considerably smaller than the estimated uncertainty of 0.31 cm s^{-1} .

Table 2 indicates that, on average, the ozone and total water methods derive entrainment rates that are about one-third smaller than those from DMS and the subsidence and growth method. This might be explained by the fact that the measurement of the free-tropospheric boundary condition usually occurred at a level well above that which was actually in reach of the engulfing eddies feeding the entrainment process. Therefore, due to the general trend of decreasing water vapor and increasing ozone in the free troposphere above the inversion, our measurements of the jump, as determined from the scalar concentrations at the altitude of the radar leg, could lead to a systematic underestimate in the entrainment velocity. Moreover, because the region was only sampled thoroughly once during each flight, it was subject to differential advection before and after its characterization, which may have introduced additional random errors to those discussed above. To estimate the magnitude of the systematic error due to vertical gradients, a linear fit was made to all of the mean profiles from just above the inversion top to the altitude of the radar leg. Then an adjustment to the jump was calculated based on the distance between the inversion and the radar leg, and the average slope in this interval. Because the ozone profiles are highly variable over the 75–450 m above the inversion that the radar legs were flown, the error estimates were widely scattered, but for the water vapor profiles this mean structure always increased the observed jump over what it would be near the inversion. The estimates of the water vapor bias ranged from 10% to 30%, which is in approximate accord with the average discrepancy relative to the DMS method.

Another possible source of systematic error in the q_i method could derive from the use of the in situ drizzle estimates in adjusting the total water fluxes. Significant

drizzle was observed on all but two flights and determination of this water flux may be subject to systematic biases (van Zanten et al. 2005), for example, in extrapolating the droplet spectrum to large drops.

b. Comparison of methods

Figure 6 shows the entrainment velocities derived from the ratio method for each of the three scalars, in addition to those from the subsidence and STBL growth method for the seven flights and includes their estimated $1\text{-}\sigma$ random errors (as listed in Table 2). Because the DMS concentration was always observed to be very close to zero above the boundary layer (Fig. 2), the estimate from this scalar is considered the most unequivocal; however, due to the aforementioned strong horizontal gradients, the mean STBL concentrations are somewhat less precise than for the other scalars, which exhibited less relative mesoscale variability. Ultimately, however, we believe that gradients in the vertical are more detrimental in introducing error, especially in an experiment of this nature. By virtue of the fact that so much time was spent sampling within the STBL, the strong horizontal gradients therein, which predominate the errors in the DMS technique, were better constrained and were purely random. On the other hand, the ambiguity introduced by insufficiently sampling the entrainment source region for ozone and water, amplified by uncertainty in exactly where that region resides and its temporal variability, lead to greater uncertainty in the values derived from these scalars. This conclusion is supported by the fact that the best agreement between the three scalar methods is found in RF05 when the radar leg was flown the nearest to the mean inversion height (only 75 m above).

c. Extenuating cases

Assuming that the DMS-derived estimates are indeed the most unequivocal helps to point to some anomalies in the other two scalars that were corrected for in the final analysis presented in Table 2 and Fig. 6. For instance, during RF03 the positive ozone flux divergence, in conjunction with the positive observed jump, leads to a negative entrainment velocity. Scrutiny of each individual ozone profile sampled throughout the course of the night, however, reveals a very thin ($<100 \text{ m}$) lamina of depleted ozone sliding in just above the STBL top while the aircraft was sampling fluxes below during the first 2.75 h on station. This apparent anomaly underscores the caution that must be exercised in the use of a long-lived and vertically stratified scalar such as ozone for measuring entrainment velocities. Figure 7a illustrates the altitudes of the C-130

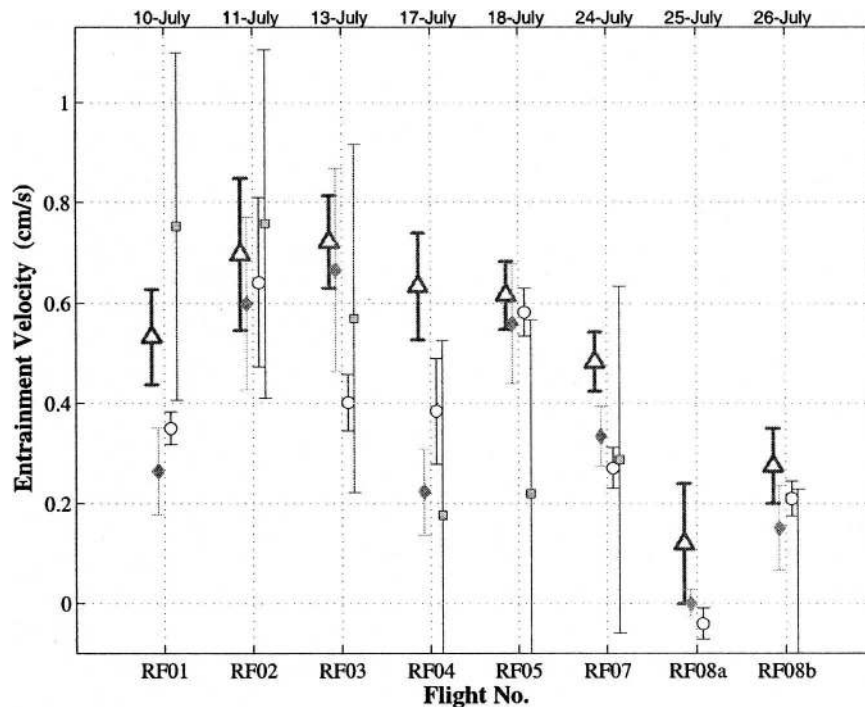


FIG. 6. Entrainment velocities and $\pm 1\sigma$ measured using the three different scalars, DMS (upward triangles), ozone (diamonds), total water (open circles), and the boundary layer growth rate minus subsidence method (squares) for the seven Lagrangian flights of DY-COMS-II. The error bars represent the propagation of all random errors as described in the text.

during RF03 and the time-dependent ozone profiles observed (Figs. 7b–g). Although the flight pattern was Lagrangian within the STBL, the wind shear across the inversion was large enough to advect a distinct layer of reduced ozone over the sample region, making the jump negative for the first part of the flight and leading to upward fluxes of ozone throughout the boundary layer. Accordingly, we use the linear extrapolation of the fluxes obtained during the first four legs and estimate the jump from an average of the profiles measured, while the depleted layer resided directly above the inversion. This leads to a much closer agreement with the entrainment velocity derived from DMS; nevertheless ambiguities in the exact value of the jump cast doubt on the accuracy of using ozone in determining the entrainment.

A very similar episode occurred on the next flight, RF04, where the ozone profile changed from a negative jump to a positive jump during the course of the flight. Because the jump was not well sampled during the first half, we use the measured jump from the usual above-cloud radar leg, but estimate the flux profile from only those fluxes measured during the second half of the flight (two near cloud top and two near the surface). In

this case, the entrainment velocity is still not in very good agreement with those derived from DMS.

The final scalar anomaly was noticed in RF05 wherein the above-cloud leg detected a very strong horizontal gradient in both O_3 and q , almost directly coaligned with the wind. While the directional wind shear measured in RF05 was negligible, the free-tropospheric wind speed was on average 4.7 m s^{-1} slower than in the boundary layer (this was the greatest magnitude of wind shear observed of all the flights). The northwest half of the circular leg possessed high O_3 (54 ppbv) and low q (1.5 g kg^{-1}), and the sharply defined, diametrically opposed semicircle averaged only 14 ppbv ozone and 7.5 g kg^{-1} water vapor. Despite the usual large horizontal gradients within the boundary layer, the DMS measured during this above-cloud leg was consistently near zero and consequently indicated no horizontal gradient aloft whatsoever. The relative wind speed would have allowed for the other scalar gradients, however, to advect 38 km during the interval between first arriving at the study area and the radar leg (8000 s) when the gradient was sampled above the cloud. Thus for the majority of the fluxes measured, the air above the inversion was best represented by the

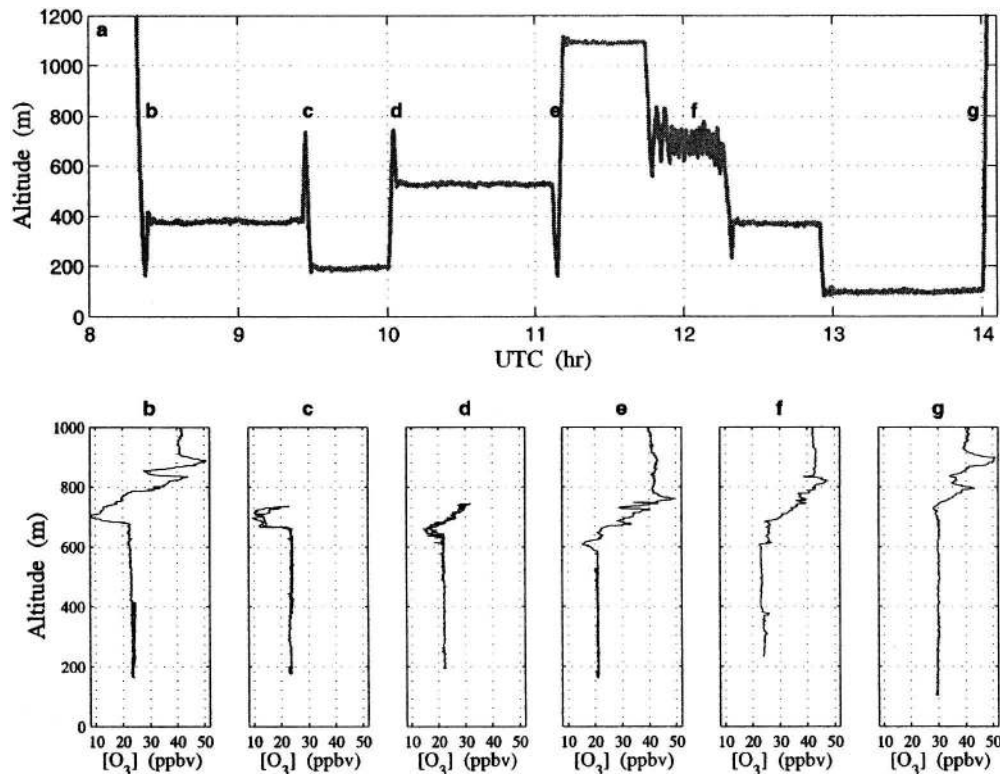


FIG. 7. (a) Time series of altitude flow while on station during RF03 and (b)–(g) vertical profiles of ozone measured throughout the flight showing the strong temporal dependence in the vertical structure of ozone above the inversion.

northwest side of the radar leg. In fact, defining the jump thusly brings the entrainment velocities into remarkable agreement with that derived from DMS. We include the near-surface legs in the flux profiles, despite their being sampled last, because they arise predominantly due to the surface fluxes and are not strongly influenced by the entrainment fluxes at the top of the STBL.

d. Functional dependence

Figure 8 shows the measured entrainment velocities, scaled by the convective velocity, from each of the seven flights versus the buoyancy Richardson number defined in Eq. (8). Unlike past observational studies (Nicholls and Turton 1986; de Roode and Duynkerke 1997), the relatively large range of Richardson numbers (~ 130 – 900) allows for a reasonable test of the functional dependence. The scaled entrainment velocities measured by Nicholls and Leighton (1986), using total water, and de Roode and Duynkerke (1997), using a combination of ozone, total water, and equivalent potential temperature, show a high degree of scatter ranging 4 – 18×10^{-3} within the span from 100 to 300 in

Richardson number. Kawa and Pearson (1989a) report entrainment velocities from the first DYCOMS experiment in the same general region of the eastern Pacific, (obtained from ozone and total water), which range from 0.1 to 0.5 cm s^{-1} for daytime stratocumulus, in reasonable agreement with our daytime flight, RF08. There is tremendous scatter in the other observational data in the literature and, despite our measurements being made at night when the STBL is most convectively active, our entrainment rates, in general, appear lower. Nevertheless, the estimates of uncertainty in the other studies have been somewhat qualitative and for the most part their lower bounds overlap the general values from DYCOMS-II. The solid triangles denote flights that exhibited conditions conducive to cloud-top entrainment instability (CTEI), a thermodynamic state wherein entrainment of dry and (relatively) cool air above the STBL could spark a positive feedback leading to rapid cloud dissipation (discussed further in section 5). Our observations indicate that there does not appear to be any systematic enhancement of the entrainment rates under such conditions.

The dashed line in Fig. 8 is the hyperbola of the form $w_e/w_* = 1.0\text{Ri}_{w_*}^{-1}$. The coefficient suggested by Nicholls

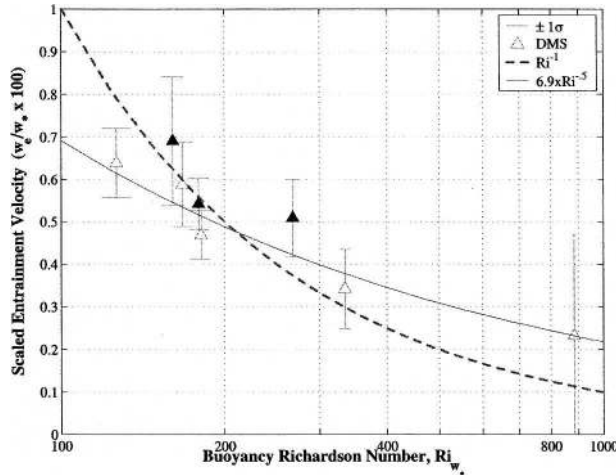


FIG. 8. Scaled entrainment velocities (triangles) derived from DMS vs the buoyancy Richardson number. The dashed line is a functional fit of a hyperbola and the thin solid line is an inverse square root relationship with Ri_{w*} . The solid markers represent the flights on which the Randall–Deardorff CTEI criterion was definitively met.

and Turton (1986) is 2.5 and is more consistent with the larger values of the other datasets. While the reciprocal relationship agrees fairly well with our data, we feel there is sufficient accuracy in the present entrainment rate measurements to support the claim of a more gradual dependence on the buoyancy Richardson number. The inverse relationship comes from one of several parameterizations of the turbulent kinetic energy (TKE) budget equation (Driedonks 1982), which assumes a balance between buoyancy forcing and flux convergence near the inversion. Although by no means definitively, our data is best fit by the curve,

$$w_e/w_* = 0.069 Ri_{w*}^{-1/2}, \quad (9)$$

which is represented by the solid line in Fig. 8. Such an inverse square root relationship has been obtained from parameterizations of shear driven entrainment (Tennekes and Driedonks 1981) and may be indicative of the influence of wind shear during DYCOMS-II. Based on aircraft observations in marine stratocumulus, Brost et al. (1982) suggest that wind shear may play an important role in the TKE budget near the inversion; however, the linear correlation coefficient between the entrainment rates and the wind shear across the inversion for the seven Lagrangian flights from DYCOMS-II is only 0.35.

In the process of nondimensionalizing the entrainment rate, we realize that we may be inducing some sort of correlation between the two dimensionless variables because they both contain the convective-scale velocity,

w_* . Hicks (1978) warned against spurious correlations that may arise from such data analysis techniques, but to our knowledge no systematic approach to this problem has been outlined in the meteorological literature. In the present case it may in fact reduce the fit to the inverse relationship between the two variables. The greatest correlation in the dataset is found between the inverse square root of the buoyancy Richardson number, a dimensionless quantity, and the entrainment velocity itself (not plotted). A weighted, linear least squares fit of these variables yields w_e (cm s^{-1}) = $11.4/\sqrt{Ri} - 0.29$ with an r^2 value of 0.89. We suggest that perhaps this simple relationship is best for modeling parameterizations of the entrainment velocity.

5. Engulfment length scales and CTEI

If one assumes that the entrainment rates derived from the DMS measurements are the most accurate, then the complexity of vertical structure in the ozone and total water profiles may be exploited to glean insight into the spatial scales of the entrainment process. Aside from the possible biases in the ozone and water techniques discussed above, the specific example presented in Fig. 7 further demonstrates that the entrainment process is limited in its vertical extent, and it leads one naturally to wonder whether the vertical range of entrainment can be quantitatively ascertained. Figure 9 shows an example of the median vertical profiles of both virtual potential temperature and ozone calculated from all of the data (filtered to 5 s^{-1}) collected on station during RF03, and illustrates graphically how this inference of spatial scale might be made. Using the entrainment rate derived from DMS in Eq. (3) and the flux at the inversion based on the ozone flux measurements, an average ozone concentration that is being incorporated into the STBL can be calculated. This concentration can be indicative of a mean height above the inversion from where free-tropospheric air is engulfed into the boundary layer. If the vertical structure above the inversion is accurately probed then the gradient can be useful in determining this engulfment height, and this methodology should be consistent between ozone and total water. Unfortunately, the relationship between mean free-tropospheric concentration and height above the inversion is not strictly one-to-one. Moreover, the vertical structure can have a strong time dependence (as illustrated in Fig. 7) and, if profiles are not consistently measured well above the inversion on regular intervals, then the inference becomes dubious. In the mean this method is not very useful because the average profiles tend to diffuse the inversion on the order of 50–100 m owing to the horizontal changes in

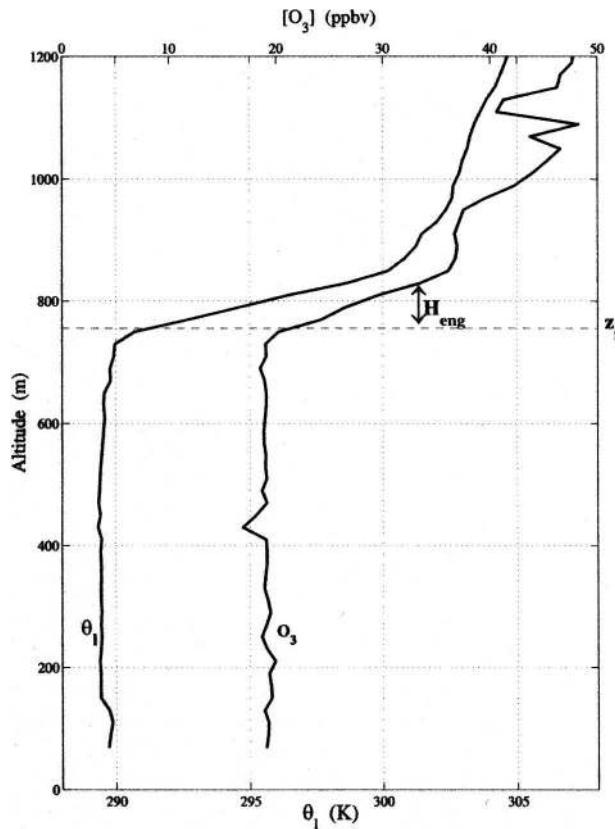


FIG. 9. Mean profiles of liquid water potential temperature and ozone from all the 5 s^{-1} data collected on station during RF01. The dashed line represents the mean inversion height, z_i , and the vertical arrow represents the height, H , along the ozone profile that satisfies the jump condition of Eq. (3).

sampling. Nevertheless, looking at many individual profiles and comparing those from ozone and total water, a general sense of this engulfment height was acquired from the data and appears to range from about 20 to 80 m above the local inversion height. We believe that with careful flight planning this sort of methodology could be used to observe the smaller-scale dynamics in future entrainment process studies.

In the present case, this method of inverting Eq. (3) can be used to tightly constrain the jump in total water across the inversion. This has bearing on a theoretical condition of the STBL known as cloud-top entrainment instability, first posited by Lilly (1968) as a possible mechanism whereby rapid breakup of marine stratocumulus could occur. The condition was later refined independently by Deardorff (1980) and Randall (1980) and many others in subsequent years (MacVean and Mason 1990; Siems et al. 1990; Duynkerke 1993). The so-called Randall–Deardorff criterion may be expressed as

$$\frac{\Delta\theta_e}{\frac{L}{C_p}\Delta Q_t} > k^* \equiv 0.23, \quad (10)$$

where $\Delta\theta_e$ and ΔQ_t are the jumps in equivalent potential temperature and total water across the inversion, respectively, L is the latent enthalpy of vaporization of water, C_p is the constant pressure heat capacity of dry air, and k^* is the instability criterion. According to the Randall–Deardorff theory, values of k greater than about 0.23 (for these conditions of potential temperature and pressure) indicate instability; that is, the air being engulfed into the STBL is cool and dry enough that significant evaporative cooling will take place upon mixing into the cloud such that a buoyancy reversal is established. Presumably this process will enhance convective mixing and the entrainment rate and, in principle, could lead to a positive feedback that acts to annihilate the cloud layer. Several observational studies have indicated that despite this condition being met there is often no observed breakup of the stratocumulus (Kuo and Schubert 1988; Siems et al. 1990; Stevens et al. 2003b). It has been noted in the past that determining the exact value of these jumps is somewhat arbitrary, though, and some confusion has remained as to the apparent discrepancy between the theory and the observations.

Again using the DMS entrainment velocity as a benchmark, an assessment of the exact total water jump may be made assuming that the flux is measured accurately. This procedure was carried out for all flights, and Eq. (10) evaluated for equivalent potential temperature jumps at 20, 40, and 100 m above the mean inversion height. As indicated by an asterisk in Table 1, three flights meet the Randall–Deardorff criterion unequivocally, independent of the altitude at which the temperature jump is defined. None of the flights during DYCOMS-II evinced signs of cloud breakup as postulated by CTEI. Thus by using the redundancy in the scalar measurements, it is shown that the discrepancy between meeting the Randall–Deardorff CTEI condition and not observing breakup of the cloud layer cannot be explained simply by ambiguities in the jump estimates.

Figure 10 shows a 1 s^{-1} time series of five in situ variables measured along 6 km of a cloud-top flight leg in RF05. The leg was flown at approximately 100 m below the mean inversion height and shows the airplane's passage through two regions of recently engulfed free-tropospheric air. The top two traces are the DMS and ozone, and both indicate that a substantial portion of free tropospheric air ($[\text{DMS}] = 0 \text{ pptv}$, and $[\text{O}_3] = 36 \text{ ppbv}$) is mixed into the cloud. The middle

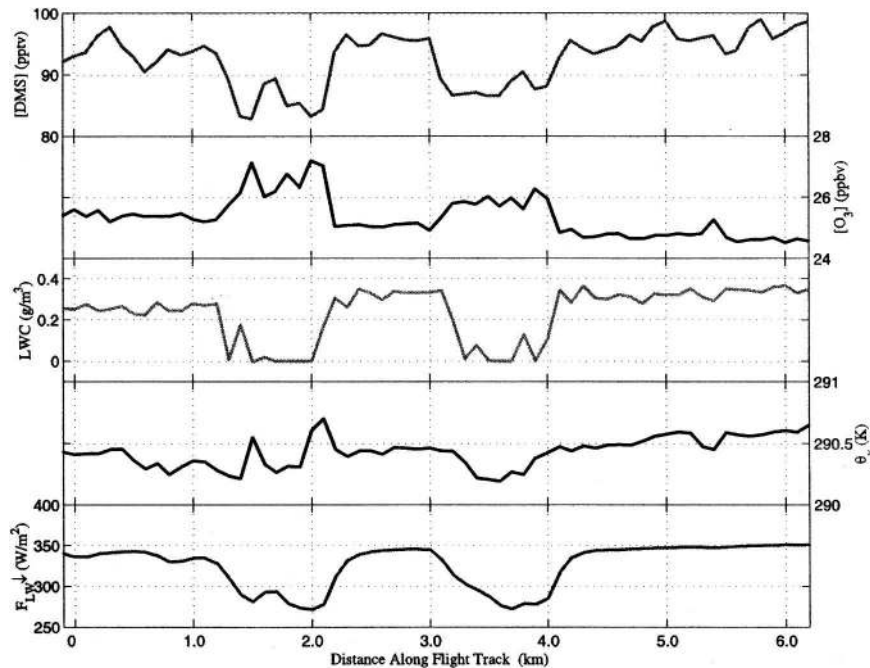


FIG. 10. Time series of 5 in situ scalars illustrating the mixing of free tropospheric air into the cloudy boundary layer and the resultant bore holes. The data are from RF05 at an altitude approximately 100 m below cloud top.

trace is the fast liquid water measurement obtained from the Gerber PVM-100 probe and shows that for these 200–800-m-wide events the cloud has completely evaporated. Also plotted is the virtual potential temperature (taking into account the mass loading of the cloud droplets), which is a proper indication of buoyancy. While the first passage seems not to indicate any definite buoyancy change, the second clearly shows that this parcel of blended free-tropospheric air is of a higher density than its immediate surroundings and thus is negatively buoyant. It is interesting to further note that the first parcel is composed of ~12% free tropospheric air (based on the DMS depletion), while the second is slightly less (~8%). Figure 11 shows the buoyancy of mixtures as a function of the fractional mass of free tropospheric air, χ , for the thermodynamic conditions of RF05. The mixing fractions, as deduced from the unambiguous DMS jump, are consistent with the observation of the second event leading to buoyancy reversal but not the first. This example appears to demonstrate that buoyancy reversal can take place locally; however, it confirms that small-scale buoyancy reversal does not necessarily lead to runaway entrainment that can break up the macroscopic cloud layer, and further supports the conclusions of Siems et al. (1990) and others who have proposed more stringent criteria for CTEI to exist in the atmosphere.

Inspection of the first cloud hole encountered in Fig. 10 reveals that the edges are of higher mixing fraction than the more diluted core, in agreement with the structures observed by Siems et al. (1990) in their fluid tank experiments. Also, the question of the vertical structure of these mixing events can be addressed by looking at

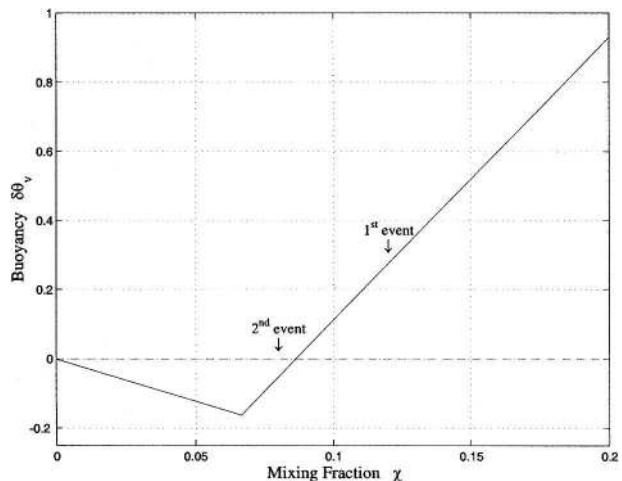


FIG. 11. Buoyancy with respect to the horizontal mean of mixtures of free tropospheric air and cloudy air. The abscissa is the mass fraction of air from above the inversion, and the estimated positions of the two events from Fig. 10 are indicated based on their DMS depletion.

the bottom trace of Fig. 10, which shows the downwelling longwave radiation sensor. The low values indicate that the air above is free of liquid water, therefore these features appear to be vertically aligned bore holes into the cloud deck. The engulfment plumes depicted in Fig. 10 are not rare and are observed on cloud-top legs frequently (approximately once every 3 km on average.) The vertical wind is not shown here because these scalar features tend to have little or no coherence with the in situ winds, indicating that they are not carrying much of the cloud-top fluxes but remain intact well after the downdraft that initiated them. We believe further scrutiny of the distributions of χ near cloud top, more accurately attainable with DMS, may shed further light on the perseverance of these stratocumulus decks in the presence of CTEI conditions.

6. Conclusions

Novel DMS eddy correlation measurements are used, in conjunction with ozone and total water, to accurately estimate the entrainment rate in seven flights investigating marine stratocumulus off of the southwest coast of California. DMS is found to be a unique tool for this type of experiment because its chemical lifetime in the atmosphere effectively limits it to the marine boundary layer and serves as an almost unambiguous marker of the boundary layer in contact with the ocean surface. Observed vertical profiles of turbulent DMS fluxes are thought to be linear with a slight modification from a chemical loss term due to its reaction in cloud droplets with dissolved ozone. The jump in DMS across the inversion is believed to be well characterized as it is only dependent on the mean concentration within the STBL (aloft the DMS is almost exclusively zero) and, therefore, it derives entrainment velocities that are not subject to complications in vertical structure, which have cast unwieldy uncertainty on past studies.

The entrainment rates ranged from 0.12 cm s^{-1} in the daytime case to 0.72 cm s^{-1} , and tend to be on the low side of observational data in the literature, particularly for nocturnal conditions. The corresponding buoyancy Richardson numbers spanned between about 130 and 900, and the relationship between scaled entrainment velocity and this nondimensional parameter appears to be one of an inverse square root, which may bespeak an important role for wind shear across the STBL inversion in determining entrainment vigor.

The redundancy of the three scalar measurements allows for an investigation into the spatial scales of the entrainment process, and a more accurate determination of scalar discontinuities across the inversion. In all cases, the vertical extent of the engulfing eddies which

ingest free-tropospheric air from above is seen to be between 20 and 80 m, but a more systematic investigation of this process and its relation to say Richardson number will require flight planning that surveys the interfacial region more carefully. In the absence of DMS flux measurements, it appears that using the total water ratio method generates the most accurate entrainment rates, while ozone tends to systematically underestimate them.

Along with the more accurate assessments of water jump across the inversion comes greater constraint on the CTEI criterion. In three of the seven flights the conditions were summarily met regardless of the choice of height above the inversion by which to define the temperature jump. These three flights further showed no signs of cloud breakup or dissipation overnight, and in RF01 the stratocumulus was even observed to thicken somewhat (Stevens et al. 2003b). In flight legs within $\sim 150 \text{ m}$ below cloud top, tendrils of cloud free air between 200 and 800 m in width were observed that possessed partial characteristics of free-tropospheric air and sometimes indicated depressed virtual potential temperatures in accord with the buoyancy reversal process. Future airborne studies of entrainment and buoyancy reversal would be aided tremendously by fast chemical measurements of the kind used here to determine unequivocally the mixing fractions and entrainment velocities.

Acknowledgments. Thanks are due to the many excellent staff members of NCAR's Research Aviation Facility including John Cowan and Kurt Zrubek for their dogged support in fabrication of the ozone chemiluminescence instrumentation. Sam Hall's untiring commitment to instrument operation and design of the data acquisition systems was indispensable. Roger Hendershot of the Atmospheric Chemistry Division was instrumental in assisting with the electronics at a very crucial time. Also, many useful discussions with Chin-Hoh Moeng, Gabor Vali, and Jordi Vilà-Guerau de Arellano were mined in the final synthesis of this manuscript. We are grateful to Bruce Morley, Mike Strong, and Eric Loew for collecting and supplying the lidar data, and to Kyoko Ikea for her preliminary analysis.

REFERENCES

- Bandy, A., D. C. Thornton, B. Blomquist, S. Chen, T. Wade, J. Ianni, G. Mitchell, and W. Nadler, 1996: Chemistry of dimethyl sulfide in the equatorial Pacific atmosphere. *Geophys. Res. Lett.*, **23**, 741–744.
- , —, F. H. Tu, B. W. Blomquist, W. Nadler, G. M. Mitchell, and D. H. Lenschow, 2002: Determination of the vertical flux

- of dimethyl sulfide by eddy correlation and atmospheric pressure ionization mass spectrometry (APIMS). *J. Geophys. Res.*, **107**, 4743, doi:10.1029/2002JD002472.
- Bretherton, C. S., P. Austin, and S. T. Siems, 1995: Cloudiness and marine boundary layer dynamics in the ASTEX Lagrangian experiments. Part II: Cloudiness, drizzle, surface fluxes, and entrainment. *J. Atmos. Sci.*, **52**, 2724–2735.
- Brost, R. A., J. C. Wyngaard, and D. H. Lenschow, 1982: Marine stratocumulus layers. Part II: Turbulence budgets. *J. Atmos. Sci.*, **39**, 818–836.
- Crutzen, P. J., M. G. Lawrence, and U. Poschl, 1999: On the background photochemistry of tropospheric ozone. *Tellus*, **51A**, 123–146.
- Deardorff, J., 1980: Stratocumulus-capped mixed layers derived from a three-dimensional model. *Bound.-Layer Meteor.*, **18**, 495–527.
- de Roode, S., and P. G. Duynkerke, 1997: Observed Lagrangian transition of stratocumulus into cumulus during ASTEX: Mean state and turbulence structure. *J. Atmos. Sci.*, **54**, 2157–2173.
- Driedonks, A. G. M., 1982: Models and observations of the growth of the atmospheric boundary layer. *Bound.-Layer Meteor.*, **23**, 283–306.
- Duynkerke, P. G., 1993: The stability of cloud top with regard to entrainment: Amendment of the theory of cloud-top entrainment instability. *J. Atmos. Sci.*, **50**, 495–502.
- Gershenson, M., P. Davidovits, J. T. Jayne, C. E. Kolb, and D. R. Worsnop, 2001: Simultaneous uptake of DMS and ozone on water. *J. Phys. Chem.*, **105A**, 7031–7036.
- Hartmann, D. L., 1998: *Global Physical Climatology*. Academic Press, 411 pp.
- Hicks, B. B., 1978: Some limitations of dimensional analysis and power laws. *Bound.-Layer Meteor.*, **14**, 567–569.
- Kawa, S. R., and R. Pearson Jr., 1989a: An observational study of stratocumulus entrainment and thermodynamics. *J. Atmos. Sci.*, **46**, 2649–2661.
- , and —, 1989b: Ozone budgets from the dynamics and chemistry of marine stratocumulus experiment. *J. Geophys. Res.*, **94**, 9809–9817.
- Kouvarakis, G., and N. Mihalopoulos, 2002: Seasonal variation of dimethylsulfide in the gas phase and of methanesulfonate and non-sea-salt sulfate in the aerosol phase in the Eastern Mediterranean atmosphere. *Atmos. Environ.*, **36**, 929–938.
- Kuo, H.-C., and W. H. Schubert, 1988: Stability of cloud-topped boundary layers. *Quart. J. Roy. Meteor. Soc.*, **114**, 887–916.
- Lee, Y. N., and X. L. Zhou, 1994: Aqueous reaction-kinetics of ozone and dimethylsulfide and its atmospheric implications. *J. Geophys. Res.*, **99**, 3597–3605.
- Lenschow, D. H., P. B. Krummel, and S. T. Siems, 1999: Measuring entrainment, divergence, and vorticity on the mesoscale from aircraft. *J. Atmos. Oceanic Technol.*, **16**, 1384–1400.
- Lilly, D. K., 1968: Models of cloud-topped mixed layers under a strong inversion. *Quart. J. Roy. Meteor. Soc.*, **94**, 292–309.
- Liu, S. C., M. McFarland, D. Kley, O. Zafiriou, and B. Huebert, 1983: Tropospheric NO_x and O₃ budgets in the equatorial Pacific. *J. Geophys. Res.*, **88**, 1360–1368.
- MacVean, M. K., and P. J. Mason, 1990: Cloud-top entrainment instability through small-scale mixing and its parameterization in numerical models. *J. Atmos. Sci.*, **47**, 1012–1030.
- Mathews, R. D., R. F. Sawyer, and R. W. Schefer, 1977: Interferences in chemiluminescent measurement of NO and NO₂ emissions from combustion sources. *Environ. Sci. Technol.*, **11**, 1092–1096.
- Nicholls, S., and J. Leighton, 1986: An observational study of the structure of stratiform cloud sheets: Part I. Structure. *Quart. J. Roy. Meteor. Soc.*, **112**, 431–460.
- , and J. D. Turton, 1986: An observational study of the structure of stratiform cloud sheets: Part II. Entrainment. *Quart. J. Roy. Meteor. Soc.*, **112**, 461–480.
- Paluch, I. R., D. Lenschow, S. Siems, S. McKeen, G. Kok, and R. Schillawski, 1994: Evolution of the subtropical marine boundary layer: Comparison of sounding over the eastern Pacific from FIRE and HaRP. *J. Atmos. Sci.*, **51**, 1465–1479.
- Pearson, R., 1990: Measuring ambient ozone with high sensitivity and bandwidth. *Rev. Sci. Instrum.*, **61**, 907–916.
- Platt, U., G. LeBras, G. Poulet, J. P. Burrows, and G. Moortgart, 1990: Peroxy radicals from nighttime reaction of NO₃ with organic compounds. *Nature*, **348**, 147–149.
- Randall, D. A., 1980: Conditional instability of the first kind upside-down. *J. Atmos. Sci.*, **37**, 125–130.
- Ridley, B. A., 1978: Measurements of minor constituents in the stratosphere by chemiluminescence. *Atmos. Technol.*, **9**, 27–34.
- , F. E. Grahek, and J. G. Walega, 1992: A small, high-sensitivity, medium-response ozone detector suitable for measurements from light aircraft. *J. Atmos. Oceanic Technol.*, **9**, 142–148.
- Schubert, W. H., J. S. Wakefield, E. J. Steiner, and S. K. Cox, 1979: Marine stratocumulus convection. Part II: Horizontally inhomogeneous solutions. *J. Atmos. Sci.*, **36**, 1308–1324.
- Siems, S. T., C. S. Bretherton, M. B. Baker, S. Shy, and R. Breidenthal, 1990: Buoyancy reversal and cloud-top entrainment instability. *Quart. J. Roy. Meteor. Soc.*, **116**, 705–739.
- Stevens, B., and Coauthors, 2003a: Dynamics and chemistry of marine stratocumulus—DYCOMS-II. *Bull. Amer. Meteor. Soc.*, **84**, 579–593.
- , and Coauthors, 2003b: On entrainment rates in nocturnal marine stratocumulus. *Quart. J. Roy. Meteor. Soc.*, **129**, 3469–3493.
- Tanner, D. J., and F. Eisele, 1995: Present OH measurement limits and associated uncertainties. *J. Geophys. Res.*, **100**, 2883–2892.
- Tennekes, H., and A. G. M. Driedonks, 1981: Basic entrainment equations for the atmospheric boundary layer. *Bound.-Layer Meteor.*, **20**, 515–531.
- Turton, J. D., and S. Nicholls, 1987: A study of the diurnal variation of stratocumulus using a multiple mixed layer model. *Quart. J. Roy. Meteor. Soc.*, **113**, 969–1009.
- van Zanten, M. C., B. Stevens, G. Vali, and D. H. Lenschow, 2005: Observations of drizzle in nocturnal marine stratocumulus. *J. Atmos. Sci.*, **62**, 88–106.
- Watts, S. F., 2000: The mass budgets of carbonyl sulfide, dimethyl sulfide, carbon disulfide and hydrogen sulfide. *Atmos. Environ.*, **34**, 761–779.